Chinese Chemical Letters 37 (2026) 110623

Contents lists available at ScienceDirect

Chinese Chemical Letters

journal homepage: www.elsevier.com/locate/cclet

Super-hybrid transition metal sulfide nanoarrays of NiS nanoparticle/WS_2 nanosheet/Ni_3S_4 nanoparticle with abundant plane- and edge-type active interfaces for robust all-pH hydrogen evolution

Teng Long[a,*], Haiqing Wang[b,*]

[a] School of Materials Science & Engineering, Shandong University, Ji'nan 250061, China
[b] Institute for Advanced Interdisciplinary Research (iAIR), School of Chemistry and Chemical Engineering, University of Jinan, Ji'nan 250022, China

ARTICLE INFO

Article history:
Received 21 October 2024
Revised 5 November 2024
Accepted 7 November 2024
Available online 8 November 2024

Keywords:
Transition metal sulfide
Super-hybrid structure
NiS/WS_2/Ni_3S_4
All-pH hydrogen evolution
Electrocatalysis

ABSTRACT

Transition metal sulfides (TMSs) are primitive composition of biocatalysts that are active for molecular hydrogen production. The development of non-precious TMSs with appropriate spatial ordering has great potentials to contribute high-level hydrogen generation. Herein, super-hybrid transition metal sulfide nanoarrays of NiS nanoparticle/WS_2 nanosheet/Ni_3S_4 nanoparticle (Super-NiS/WS_2/Ni_3S_4) with high spatial ordering and abundant plane- and edge-type WS_2_NiS and WS_2_Ni_3S_4 heterointerfaces were elaborately constructed though manipulating the sequential dissociation of phosphotungstic acid (PW_{12}) as W precursor and nickel foam as Ni precursor in one pot. When evaluated for the electrocatalytic hydrogen evolution reaction (HER), the Super-NiS/WS_2/Ni_3S_4 only required overpotentials of 57, 95, and 151 mV to drive HER in alkaline, acid, and neutral media, respectively, and presented favorable reaction kinetics and test stability. The theoretical and experimental results verify the adsorption and dissociation of water molecules are preferential on WS_2-plane-related heterointerfaces. The Gibbs free energy (ΔG_{H^*}) analysis indicated the WS_2-plane-NiS interface is thermodynamically optimal for HER. Moreover, the collaborations of the abundant plane- and edge-type active interfaces, the open nanosheet-based vertical array, and the phosphorus doping in Super-NiS/WS_2/Ni_3S_4 strengthen mass transport and electron transfer in electrocatalysis. The polyoxometalates-based synthetic strategy will inspire the new vision for the rational design and construction of advanced functional materials.

© 2025 Published by Elsevier B.V. on behalf of Chinese Chemical Society and Institute of Materia Medica, Chinese Academy of Medical Sciences.

As the installed capacity of wind and light power soars, more and more problems are gradually emerging [1,2]. Especially, the characteristics of randomness and intermittency of wind and light power result in the generations of large-scale uncontrolled low-quality power and the serious abandonment problem [3,4]. Hydrogen energy is recognized as a clean energy carrier with high energy density, high conversion efficiency, and zero carbon emissions [5,6]. The conversion of wind and light energy into usable hydrogen energy by electrochemical water splitting becomes an attractive and profitable way to the maximized and multi-channel utilizations of renewable energy. However, the benchmark electrocatalysts for hydrogen evolution reaction (HER) are still noble platinum-based materials and the future industrial applications are severely discouraged by their scarcity and prohibitive cost. The development of earth-abundant alternatives with delightful performance is consequentially desirable. Moreover, considering pH fluctuations under operating conditions as well as the ease and cost of electrocatalyst production, the HER electrocatalysts that are versatile for different pH scenarios could be more important [7–9]. Therefore, the physical and electronic structure of electrocatalyst materials should be elaborately designed to simultaneously fulfill the adsorption/desorption/dissociation processes of reactant (H_2O)/intermediate (OH^- and H^*) species involved in electrochemical water splitting, which is still challenging.

Transition metal sulfides (TMSs) are found as the key structural/component motif in nature nitrogenase and hydrogenase [10–12]. The corresponding exploitations of low-cost TMSs-based electrocatalyst have been extensively expanded. The performance improvement strategies including intrinsic and extrinsic interface/surface/composition modulation and morphology control have been executed for layered WS_2 and MoS_2 as well as nonlayered Zn/Co/Cu/Fe/Ni_xS_y [13–22]. However, the inherent shortcomings of TMSs in mediating the HER should be overcame with purpose.

* Corresponding authors.
E-mail addresses: tenglong@sdu.edu.cn (T. Long), ifc_wanghq@ujn.edu.cn (H. Wang).

https://doi.org/10.1016/j.cclet.2024.110623
1001-8417/© 2025 Published by Elsevier B.V. on behalf of Chinese Chemical Society and Institute of Materia Medica, Chinese Academy of Medical Sciences.

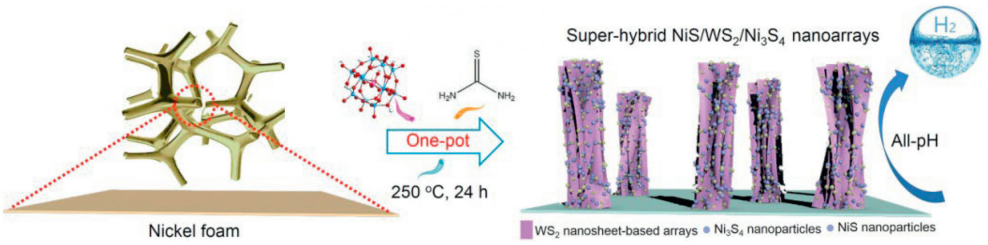


Fig. 1. Illustration for the preparation route of Super-NiS/WS_2/Ni_3S_4.

First, metallic conductivity is a prerequisite for electrical energy utilization. However, most of TMSs exhibited semiconductor-like high resistance in electrochemical application due to the presence of a decent band gap [23–25]. Second, taking layered WS_2/MoS_2 as examples, the theoretical and experimental results demonstrated that the edge (basal plane) of WS_2/MoS_2 are (not) active sites for HER [1,26–28]. Unfortunately, the percentage of the edge sites in the whole WS_2/MoS_2 layer is extremely limited. Thus, the cooperative manipulations of the accessibility of the edge sites and the activation of the basal plane sites are effective pathways to promote the HER activity, which are highly dependent on the structure design of TMSs. Third, the HER electrocatalysts with high tolerance to the pH of electrolyte are desirable from the perspectives of technological cost, efficiency, and working condition [29,30]. However, it is usually assumed that TMSs do not have the ability to dissociate water in neutral and alkaline media, which may explain why TMSs have been rarely reported for HER among all pH [31–34]. Moreover, following the widely established criterion, *i.e.*, ΔG_{H^*} (the free energy of H adsorption) [35], the pure TMS generally showed a poor ΔG_{H^*} far from the ideal zero value of the baseline Pt [36–39]. Taken together, the issues identified above pose systemic challenges for the physical and chemical modifications of TMSs aiming at developing high-performance and multi-functional HER electrocatalysts.

With these points in mind, we elaborately manipulate the sequential hydrolysis of W and Ni sources to construct super-hybrid metal sulfide nanoarray comprising P doped WS_2 nanosheets, NiS and Ni_3S_4 nanoparticles. The super-hybrid nanosheet arrays exhibited abundant plane- and edge-type WS_2_NiS and WS_2_Ni_3S_4 heterointerfaces, which were proved to be robust for electrocatalytic HER under all-pH electrolytes. The density functional theory (DFT) result indicated that WS_2-plane-related heterointerfaces could be more active for water dissociation and hydrogen adsorption, thus leading to the activity promotion. Moreover, the open super-hybrid nanosheet array and the P doping enable the unobstructed active heterointerfaces and facilitate the electron transfer as well as the mass transport during HER. This study presents an effective strategy for arming TMS-based materials in electrocatalysis application.

The schematic illustration for the synthesis procedure was given in Fig. 1. Recently, many instances have reported that POMs with precise cluster structures and convenient preparation are promising precursors for the preparation of functional materials at an atomic/molecular scale. POMs can not only supply abundant transition metals and the inherent heteroatoms doping, but also display controllable dissociation kinetics for constructing functional materials. The synergy of POMs and other metal precursors is highly valuable and provides an emerging vision for advanced catalyst materials. The super-hybrid transition metal sulfide nanoarrays of NiS nanoparticle/WS_2 nanosheet/Ni_3S_4 nanoparticle (Super-NiS/WS_2/Ni_3S_4) with high spatial ordering and abundant plane- and edge-type WS_2_NiS and WS_2_Ni_3S_4 heterointerfaces were elaborately constructed though one-pot hydrothermal sulfidation. Typically, Ni foam was applied as both Ni source and three-dimensional hard template. Polyoxometalates (phosphotungstic acid, PW_{12}) functioned as W and P precursors. The synthetic kinetics were modulated by the optimized reaction concentration and temperature. As a result, the Ni and W sources were sequentially dissociated to form WS_2 nanosheet-based array and NiS/Ni_3S_4 nanoparticle.

The XRD pattern of Super-NiS/WS_2/Ni_3S_4 is given in Fig. 2a. The signal peaks of initial nickel foam disappear (Fig. S1 in Supporting information), indicating the total transformation of nickel foam into nickel sulfide after hydrothermal reaction. The peaks at $2\theta = 14.3°$, 33.4°, and 39.5° indicated the presence of (002), (101), and (103) planes in hexagonal WS_2 (JCPDS card No. 02–0331). The observable signals at $2\theta = 32.3°$, 35.9°, 40.6°, and 48.9° are well matched with the (300), (021), (211), and (131) planes of NiS (JCPDS card No. 02–1443). The diffraction peaks presented at $2\theta = 31.3°$, 37.9 °, 49.9°, and 54.8° are readily indexed to the (113), (004), (115) and (044) planes, respectively, of cubic Ni_3S_4 (JCPDS card No. 43–1469). The sample prepared without PW_{12} was used as a reference to analyze the role of WS_2, and its XRD pattern indicated the co-existence of NiS/Ni_3S_4 (Fig. S2 in Supporting information). In order to compare the structural merits, the normal NiS/WS_2/Ni_3S_4 was also prepared with Na_2WO_4 as W source, as indicated in Fig. S3 (Supporting information). The highly uniform surface structure of Super-NiS/WS_2/Ni_3S_4 was clearly recorded by scanning electron microscopy (SEM) images (Figs. 2b–f). Strictly speaking, the Super-NiS/WS_2/Ni_3S_4 presented nanosheet-based 'rod-like' array with uniform spatial distribution throughout the three-dimension framework (Figs. 2b and c). Each 'rod' is composed of countless vertically growing WS_2 nanosheets and exhibits a size of 1.0 μm in width and 10 μm in height (Fig. 2d). The soft feature of WS_2 nanosheets tends to form porosity, which can provide abundant accessibility for mass transport in reactions. High-magnification SEM image demonstrated the existence of spreading NiS/Ni_3S_4 nanoparticles decorated on the surface of WS_2 nanosheets (Figs. 2e and f). The visible scene implies the strong coupling among the WS_2 nanosheets. The intimate conjunction between WS_2 nanosheets and the NiS/Ni_3S_4 is expected. In addition, this 'rod-like' nanosheet array also contribute the complete exposure of active planes and edges in Super-NiS/WS_2/Ni_3S. The transmission electron microscopy (TEM) image was used to give subtle structure of Super-NiS/WS_2/Ni_3S_4. The low-magnification TEM image (Fig. 2g) verified the composition of hierarchical cross-linked nanosheets and the surface-modified nanoparticles in targeted sample. The high-resolution TEM images indicated the presence of nanoparticles on the plane and the edge of nanosheet (Fig. 2h). The nanosheet has a lattice distance of 0.62 nm and about 5 layers in thickness, verifying the feature of laminar WS_2. The lattice spacing of 0.33 nm, 0.29 nm and 0.24 nm are well matched with the (022), (101) and (220) facets of Ni_3S_4 and NiS, respectively. The scanning transmission electron microscopy (STEM) image (Fig. 2i) further confirmed the 'rod-like' nanosheet assembly structure. The elemental mapping image from energy-dispersive X-ray (EDX) spectroscopy discloses the distribution of W, Ni, S, and P elements in Super-NiS/WS_2/Ni_3S_4. Specifically, a close observation of EDX mapping in Fig. 2j indicated

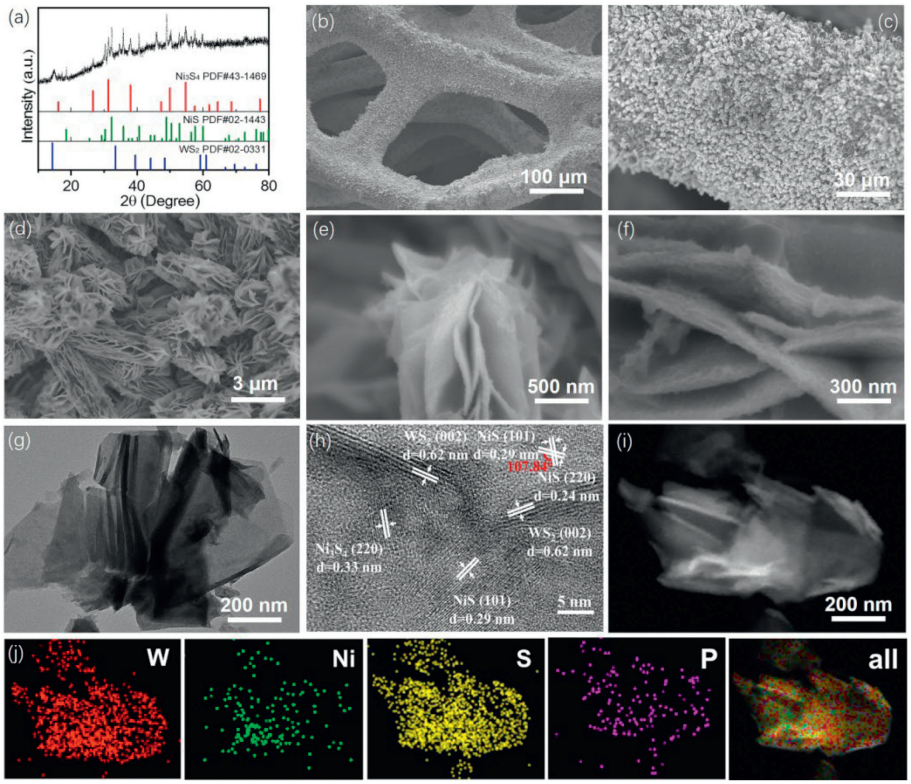


Fig. 2. (a) XRD pattern. (b-f) SEM images taken at different magnifications and from different perspective. (g) Low- and (h) high-magnification TEM images. (i) STEM image. (j) EDX elemental mapping of Super-NiS/WS_2/Ni_3S_4.

that the mapping of P and W elements are matched well. The result implies that P element from phosphotungstic acid (PW_{12}) should be retained and mainly doped in WS_2 nanosheet with 0.29 wt% content (Fig. S4 in Supporting information). The promotion of intrinsic conductivity of WS_2 nanosheet can be predicted owing to the P doping. The aforementioned images demonstrate that the constructed Super-NiS/WS_2/Ni_3S_4 has the characteristic of elaborate heterogeneous interfaces comprising Ni_3S_4 and NiS nanoparticles-decorated plane and edge of hierarchical WS_2 nanosheet. The observations are also consistent the surface texture observed in the SEM image (Fig. 2c) and the XRD signals. The reference NiS/Ni_3S_4 is only evolved from nickel foam and shows unromantic porous skeleton morphology (Fig. S5 in Supporting information). The NiS/WS_2/Ni_3S_4 prepared with Na_2WO_4 as W source exhibited flower-like nanosheet structure (Fig. S6 in Supporting information). By contrast, the PW_{12} as precursor demonstrated a special role in modulating the formation, growth, and assembly behaviors of WS_2 nanosheets, thus mediating the sequential construction of super-hybrid NiS nanoparticle/WS_2 nanosheet/Ni_3S_4 nanoparticle structure.

The compositions and chemical valences of Super-NiS/WS_2/Ni_3S_4 (shorted as Super-NiWSP), NiS/WS_2/Ni_3S_4 (shorted as NiWS), and NiS/Ni_3S_4 (shorted as NiS) were analyzed by X-ray photoelectron spectroscopy (XPS). The XPS spectra of Ni $2p_{3/2}$ in Super-NiWSP, NiWS, and NiS were given in Fig. 3a. The peaks located at 853.2, 856.9, and 862.0 eV are consistent with Ni^{2+}, Ni^{3+}, and satellite signals, respectively [40–42]. The S 2p spectrum in Fig. 3b displayed two spin-orbit doublets of $2p_{3/2}$ and $2p_{1/2}$ at 161.8 eV and 163.5 eV, respectively, corresponding to the Ni-S and W-S chemical bonds [43–45]. As shown in Fig. 3c, multiplet peaks are clearly observed for XPS spectrum of W 4f between 30 eV and 40 eV The W 4f signal can be deconvoluted into WS_2 (31.8 and 33.9 eV), WS_3 (35.7 eV) and WO_3 (37.9 eV) peaks [43,46,47]. The existence of P doping in Super-NiWSP was evidenced by the signal

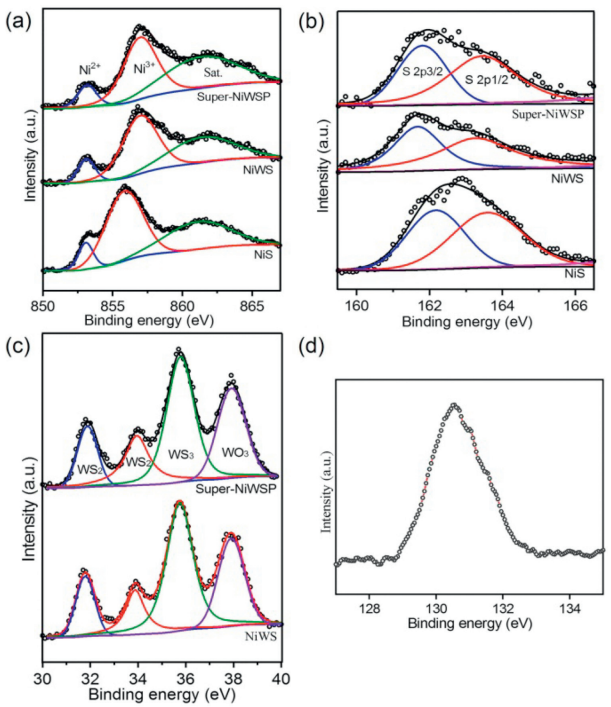


Fig. 3. Elemental XPS spectra of (a) Ni 2p and (b) S 2p in Super-NiWSP, NiWS, and NiS. (c) W 4f in Super-NiWSP and NiWS. (d) P 2p in Super-NiWSP.

in Fig. 3d [48–50]. The XPS result indicated P content of 2.85 at%. The EDX and XPS analyses suggested the P doping in the resultant Super-NiWSP. The XPS peak positions among Super-NiWSP and the reference NiWS and NiS are analyzed in order to obtain impor-

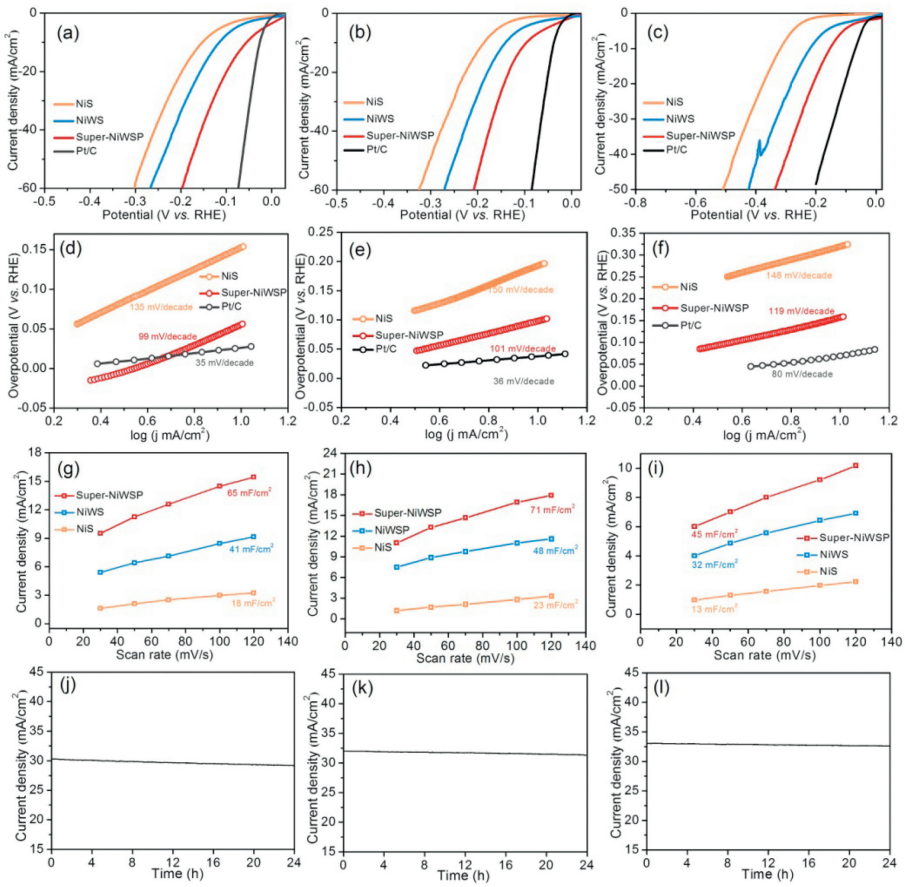


Fig. 4. HER performance tests of Pt/C, super-NiWSP, NiWS, and NiS samples. The first/second/third/fourth row corresponds to the plots of polarization, Tafel, ECSA, and stability, respectively. The first/second/third column means the test electrolytes of 1 mol/L KOH (a, d, g, and j), 0.5 mol/L H_2SO_4 (b, e, h and k), and 1 mol/L PBS (c, f, i, and l).

tant information about the interface interaction. The peak positions of Ni 2p, W 4f, and S 2p in Super-NiWSP and NiWS showed obscure shift, indicating that the retained P doping in Super-NiWSP leaded to negligible change in chemical valences of Ni, W, and S in comparison with NiWS. Therefore, the performance differences between Super-NiWSP and NiWS described later should origin from the differences in intrinsic structures. Compared with pure NiS sample, the binding energy of Ni $2p_{3/2}$ in Super-NiWSP is upshifted by about 0.9 eV The metals with higher valence were supposed to be active for water dissociation [1]. On the contrary, the S peak (161.8 eV) in Super-NiWSP exhibited a blue shift by 0.5 eV in comparison with 162.3 eV of NiS. The finding suggested that the existences of notable electron transfer from NiS/Ni_3S_4 side to WS_2 and the strong electronic interactions between WS_2 and NiS/Ni_3S_4, implying highly coupled interface in Super-NiWSP. The frontier orbital states of TMS are expected to be well manipulated towards favorable adsorption modulation for reaction intermediates [1,4].

The electrocatalytic HER activities of super-NiWSP, NiWSP, and NiS were estimated under all pH (pH 0, 7, and 14) electrolytes. The linear sweep voltammetry (LSV) curves in alkaline, acid, and neutral media were provided in Figs. 4a–c, respectively. The benchmark Pt/C displayed the lowest overpotential of 26/37/68 mV to actuate the current density of 10 mA/cm^2 for hydrogen evolution in alkaline/acid/neutral electrolytes. The reference NiWS and NiS needed corresponding 115/141/221 mV and 152/185/318 mV overpotentials at 10 mA/cm^2 to realize HER. By contrast, the Super-NiWSP exhibited a dramatic promotion for HER activity, which only requires 57/95/151 mV overpotentials at 10 mA/cm^2 to drive hydrogen evolution under alkaline/acid/neutral environments. Moreover, the activity of Super-NiWSP is also comparable to some of the recently reported data from TMSs-based electrocatalysts [1,4] in alkaline electrolyte (η@10 mA/cm^2, edge-rich WS_2–136 mV, Ni_3S_2–223 mV, NiS_2–148 mV, CoS_2–193 mV, $Ni_xCo_{3-x}S_4$–Ni_3S_2–136 mV, MoS_2/Ni_3S_2–110 mV, $Mo_{(1-x)}W_xS_2$@Ni_3S_2–98 mV, and Super-Co_3S_4/P-WS_2/Co_9S_8–58 mV), in acid electrolyte (η@10 mA/cm^2, N-doped WS_2–150 mV, defect-rich WS_2–145 mV, CoS_2–145 mV, $Zn_{0.3}Co_{2.7}S_4$–80 mV, $Fe_{4.5}Ni_{4.5}S_8$–146 mV, $NiCo_2S_4$/Pd-87 mV, FeNiS-105 mV, Super-Co_3S_4/P-WS_2/Co_9S_8–70 mV), and in neutral electrolyte (high-index faceted Ni_3S_2/nickle foam-170 mV, CoS_x/F-doped tin oxide(FTO)−168 mV, CoMoNiS/nickle foam-117 mV, Co_3S_4–420 mV, S-$NiFe_2O_4$/nickle foam-197 mV, $NiSe_2$/nickle foam-169 mV, $CoNi_2S_4$/WS_2/Co_9S_8–146 mV, and Super-Co_3S_4/P-WS_2/Co_9S_8–129 mV). The Tafel slopes in alkaline/acid/neutral media were given in Figs. 4d–f to analyze the hydrogen-evolution kinetics of Super-NiWSP, NiWSP, and NiS. Apart from the outstanding Pt/C, the Tafel slope values of Super-NiWSP were fitted to be 99/101/119 mV/dec for alkaline/acid/neutral HER, which is smaller than the corresponding 135/150/146 mV/dec of the typical reference NiS. The smaller Tafel slopes of Super-NiWSP demonstrate favorable hydrogen-evolving kinetics under all pH environments. Moreover, as indicated by the smaller charge transfer resistance (R_{ct}) from electrochemical impedance spectroscopy (EIS) tests (Fig. S7 in Supporting information), the NiS/Ni_3S_4 activated plane and edge of hierarchical WS_2 nanosheet and the doping of P element lead to improved intrinsic conductivity in Super-NiWSP [1,13,51]. In addition, the electrochemical surface areas (ECSA) of samples were assessed by electrochemical double layer capacitance (C_{dl}) tests, as exhibited in Figs. S8–S10 (Supporting information). Super-NiWSP provides 65/71/45 mF/cm^2 of ECSA

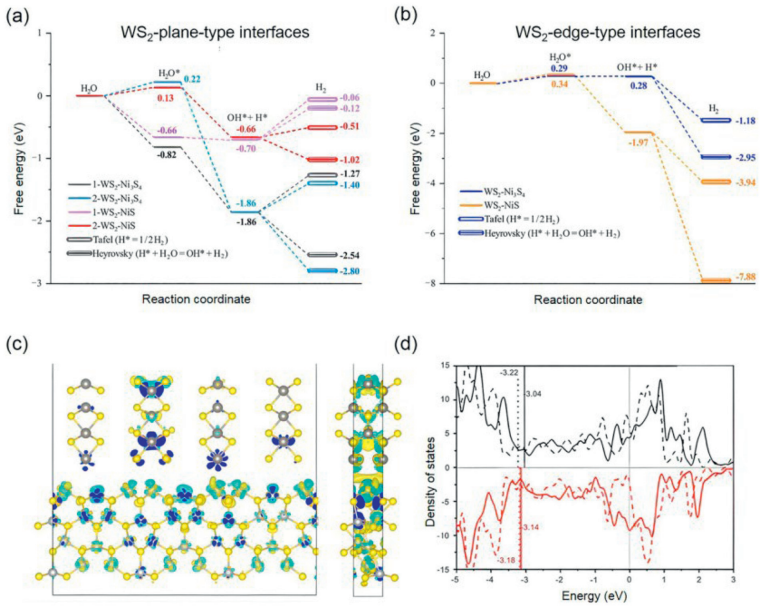


Fig. 5. The pathways of HER based on free energy calculations on (a) WS_2-plane-related and (b) WS_2-edge-related WS_2_NiS and WS_2_Ni_3S_4 heterointerfaces. (c) Calculated electron density difference plot at WS_2 (up)-plane-NiS (down) heterointerface (side views from different direction). (d) Calculated partial density of states of S in NiS before (broken line) and after (solid line) making heterointerface (red/black color means down/up-spin).

for alkaline (Fig. 4g)/acid (Fig. 4h)/neutral (Fig. 4i) HER, which is larger than 41/48/32 mF/cm^2 of NiWS and 18/23/13 mF cm^{-2} of NiS, respectively (). The vertically aligned nanosheet-based array enables the maximum exposure of the crosslinked active WS_2-plane/edge-type heterostructures, thus accounting for the promotion of electrochemical surface areas in Super-NiWSP. Furthermore, the chronoamperometric measurements (*i-t*) plots (Figs. 4j–l) of Super-NiWSP remained well at about 30 mA/cm^2 for 24 h under different pH scenarios and exhibited negligible activity attenuations, verifying the satisfying electrocatalytic stability. Taking Super-NiWSP after stability test under alkaline condition as example, the XRD pattern (Fig. S11 in Supporting information) indicates a slight decrease of the signal intensity but a good reservation of WS_2, NiS, and Ni_3S_4 crystalline phases. The SEM image (Fig. S12 in Supporting information) demonstrates that although some minor degradation is observed in surface structure, the vertically aligned nanosheet-based array structure is well remained. Taken together, the electrochemical tests confirmed the superior HER activity and stability of non-precious Super-NiWSP electrocatalysts and the favorable versatility for electrolyte condition change.

To disclose the activity origin of Super-NiS/WS_2/Ni_3S_4 for electrocatalytic HER, the additional density functional theory (DFT) calculations were provided. The models of WS_2-plane-related and WS_2-edge-related WS_2_NiS and WS_2_Ni_3S_4 heterointerfaces were established and shown in Fig. S13 (Supporting information). The free energy calculations of H_2O^* and H^* on WS_2-plane-related and WS_2-edge-related WS_2_NiS and WS_2_Ni_3S_4 heterointerfaces were exhibited in Figs. 5a and b, respectively. According to the computational results, the H_2O molecules exhibit lower adsorption energies on the WS_2 plane-related heterointerfaces (Fig. 5a) in comparison with the WS_2 edge-related heterointerfaces (Fig. 5b), implying that the H_2O was preferentially adsorbed on WS_2-plane-type heterointerfaces. Moreover, the negative changes in free energy for water dissociation indicate that the dissociation process is thermodynamically favorable for WS_2-plane-related heterointerfaces. In terms of the HER step, a lower free energy absolute value indicates a greater likelihood for hydrogen desorption [52–54]. For the WS_2-plane-NiS interface (Fig. 5a), the free energy changes for the hydrogen evolution step are 0.15 eV (Tafel) and −0.36 eV (Heyrovsky), which are closest to zero among all the catalysts studied. Thermodynamically speaking, the WS_2-plane-NiS interface exhibits the optimal hydrogen desorption behavior. The calculations indicate that WS_2-plane-related heterointerfaces own the advantages of the preferential adsorption and the thermodynamically favorable dissociation for water molecules [55–58]. Furthermore, the hydrogen desorption step at the WS_2-plane-NiS interface is thermodynamically optimal. Furthermore, the electronic properties were further explored aiming at unveiling the intrinsic activation mechanism of WS_2-plane-NiS interface. The calculated electron density difference plot at WS_2-plane-NiS heterointerfaces was given in Fig. 5c, where the yellow section is related to the electron accumulation while green region means electron depletion. It can be seen that the electrons are transferred from NiS to WS_2, which is also consistent with the XPS analysis. Thus, the holes are accumulated on NiS side and facilitate the dissociation of H_2O. The electrons enriched on WS_2 will benefit for the hydrogen evolution [59–63]. In addition, the partial density of states (DOS) of S on NiS at pristine NiS and WS_2-plane-NiS interface were demonstrated in Fig. 5d, where the p band center for up- and down-spins was calculated as well. As clearly shown, the formation of WS_2-plane-NiS interface leaded to an upraised p band center of S, remarkable band for up-spin situation. The upraised p-band implies the enhanced interactions between NiS and WS_2 in WS_2-plane-NiS interface and the favorable dissociation/adsorption/desorption processes of H_2O/H^* species involved in electrochemical water splitting, thus leading to the superior electrocatalytic activity.

In summary, we successfully constructed super-hybrid transition metal sulfide nanoarrays of NiS/WS_2/Ni_3S_4 with high spatial ordering and abundant plane- and edge-type WS_2_NiS and WS_2_Ni_3S_4 hetrointerfaces. The polyoxometalate (PW_{12}) exhibited special hydrolysis kinetics for the programmed growth and assembly of WS_2 nanosheets and NiS/Ni_3S_4 nanoparticles in one-pot synthesis. The Super-NiS/WS_2/Ni_3S_4 demonstrated superior electrocatalytic HER activity and favorable versatility under different electrolytes conditions, which only required 57/95/151 mV overpotentials to actuate 10 mA/cm^2 in alkaline/acid/neutral media. The theoretical and experimental results indicated that WS_2-plane-related heterointerfaces exhibited the favorable adsorption

and dissociation of water molecules. The WS_2-plane-NiS interface is thermodynamically optimal for hydrogen evolution judging from the Gibbs free energy (ΔG_{H^*}) values. The collaborations of the open nanosheet-based vertical array, the abundant plane- and edge-type active interfaces, and the phosphorus doping in Super-NiS/WS_2/Ni_3S_4 not only provide maximum exposure of active sites, but also strengthen mass transport and electron transfer in electrocatalysis, thereby systematically promoting water-splitting hydrogen production. Our recent findings suggest that the polyoxometalates-based precursors are versatile for synthesizing ordered TMSs aiming at energy-related applications.

Declaration of competing interest

The authors declare that they have no known competing financial interests or personal relationships that could have appeared to influence the work reported in this paper.

CRediT authorship contribution statement

Teng Long: Writing – review & editing, Writing – original draft, Software, Conceptualization. **Haiqing Wang:** Writing – original draft, Supervision, Investigation, Formal analysis, Conceptualization.

Acknowledgments

This work was supported by the financial supports from the National Natural Science Foundation of China (No. 52301016), research projects from Department of Science and Technology of Shandong Province (Nos. 2023HWYQ-043, ZR2023ME014, ZR2023QE033), The grant of Youth Innovation Team of Shandong Province (No. 2022KJ030). And the authors are grateful for the support of Key Technologies R&D Program of CNBM (No. 2023SJYL05). The authors would also like to thanks the support of Ji'nan AICC.

Supplementary materials

Supplementary material associated with this article can be found, in the online version, at doi:10.1016/j.cclet.2024.110623.

References

[1] H. Wang, J. Xu, Q. Zhang, et al., Adv. Funct. Mater. 32 (2022) 2112362.
[2] Z. Huang, T. Cheng, A.H. Shah, et al., Nat. Catal. 7 (2024) 678–688.
[3] Y. Guo, T. Park, J.W. Yi, et al., Adv. Mater. 31 (2019) 1807134.
[4] M. Ma, J. Xu, H. Wang, et al., Appl. Catal. B: Environ. 297 (2021) 120455.
[5] J. Mei, Y. Deng, X. Cheng, et al., Chin. Chem. Lett. 35 (2024) 108900.
[6] Y. Zhang, M. Shi, C. Wang, et al., Sci. Bull. 65 (2020) 359–366.
[7] J. Zhou, F. Wang, H. Wang, et al., Nano Res. 16 (2023) 2085–2093.
[8] S. Chen, T. Zhang, J. Han, et al., Nano Res. Energy 3 (2024) e9120106.
[9] Y. Da, R. Jiang, Z. Tian, et al., SmartMat 4 (2023) e1136.
[10] S. Xu, Q. Wu, B. Lu, et al., Acta Phys. Chim. Sin. 39 (2023) 2209001.
[11] G.J. Adekoya, A.C. Ezika, O.C. Adekoya, et al., BMEMat 1 (2023) e12042.
[12] Y. Sun, J. Wu, Z. Zhang, et al., Energy Environ. Sci. 15 (2022) 633–644.
[13] W. He, L. Han, Q. Hao, et al., ACS Energy Lett. 4 (2019) 2905–2912.
[14] J. Wang, G. Liu, Q. Yun, et al., Acta Phys. Chim. Sin. 39 (2023) 2305034.
[15] J. Wu, Q. Zhang, K. Shen, et al., Adv. Funct. Mater. 32 (2022) 2107802.
[16] M. Zhao, W. Li, J. Li, et al., Adv. Sci. 7 (2020) 2001965.
[17] Z. Wu, P. Yang, Q. Li, et al., Angew. Chem. Int. Ed. 62 (2023) e202300406.
[18] Y. Qian, J. Yu, F. Zhang, et al., Chem. Eng. J. 470 (2023) 144372.
[19] Z. Liu, R. Fan, Y. Zhou, et al., Inorg. Chem. Front. 11 (2024) 6998–7007.
[20] Y. Liu, Z. Zhang, L. Zhang, et al., J. Mater. Chem. A 10 (2022) 22125–22134.
[21] J. Li, G. Fu, X. Sheng, et al., Adv. Powder Mater. 3 (2024) 100227.
[22] C. Wang, Y. Long, Y. Deng, et al., BMEMat 2 (2024) e12068.
[23] C.Y. Sun, W. Li, H.Q. Wang, Rare Met. 43 (2024) 410–412.
[24] M. Hu, Y. Qian, S. Yu, et al., Small 20 (2024) 2305948.
[25] S. Hussain, D. Vikraman, M. Sarfraz, et al., Small 19 (2023) 2205881.
[26] X. Liu, Q. Yu, X. Qu, et al., Adv. Mater. 36 (2024) 2307395.
[27] T. Zhao, G. Xu, B. Gong, et al., Nano Res. 17 (2024) 282–289.
[28] F.Y. Yu, H. Sun, H.Q. Tan, et al., Chem Catal. 4 (2024) 101002.
[29] J. Lin, X. Wang, Z. Zhao, et al., Carbon Energy 6 (2024) e555.
[30] S.W. Yu, S. Kwon, Y. Chen, et al., Adv. Funct. Mater. 34 (2024) 2402966.
[31] K. Zhang, Y. Duan, N. Graham, et al., Appl. Catal. B: Environ. 323 (2023) 122144.
[32] W. Gou, H. Sun, F. Cheng, Nano Res. Energy 3 (2024) e9120121.
[33] N. Qiu, W. Lu, H.Q. Wang, Rare Met. 44 (2025) 60–80.
[34] T. Li, Y. Deng, X. Rong, et al., SmartMat 4 (2023) e1142.
[35] G. Gao, G. Zhao, G. Zhu, et al., Chin. Chem. Lett. 36 (2025) 109557.
[36] K.R.G. Lim, A.D. Handoko, L.R. Johnson, et al., ACS Nano 14 (2020) 16140–16155.
[37] S. Yu, J. Li, J. Yin, et al., Chin. Chem. Lett. 35 (2024) 110068.
[38] X. Jing, Y. Mu, Z. Gao, et al., Nano Res. Energy 3 (2024) e9120104.
[39] C.Y. Sun, W. Li, K. Wang, W.J. Zhou, H.Q. Wang, Rare Met. 43 (2024) 1845–1866.
[40] J. Yan, R. Wu, G. Jin, et al., Adv. Powder Mater. 3 (2024) 100214.
[41] J. Wu, W. Zhong, C. Yang, et al., Appl. Catal. B: Environ. 310 (2022) 121332.
[42] J. Dong, B. An, W. Liu, et al., Chem. Eng. J. 498 (2024) 155102.
[43] Q. Wu, H. Zhang, H. Liu, BMEMat 1 (2023) e12010.
[44] Z.Z. Liu, X. Shang, B. Dong, Y. Chai, J. Catal. 361 (2018) 204–213.
[45] D. Wang, J. Wu, L. Jiao, L. Xie, Nano Res. 16 (2023) 12910–12918.
[46] J.P. Yang, F.Z. Zhang, J. Chen, China Powder Sci. Technol. 30 (2024) 161–170.
[47] F. Chen, Y. Zhang, L. Hu, et al., SmartMat 4 (2023) e1193.
[48] A. Ali, F. Long, P.K. Shen, Electrochem. Energy Rev. 5 (2022) 1.
[49] Q. Han, Y. Luo, G. Liu, et al., J. Catal. 413 (2022) 425–433.
[50] D. Chinnadurai, R. Rajendiran, P. Kandasamy, J. Colloid Interfaces Sci. 606 (2022) 101–112.
[51] Y. Han, C. Yu, H. Huang, et al., SmartMat 5 (2024) e1206.
[52] Y. Yu, G. Liu, S. Jiang, et al., Nano Res. 16 (2023) 10742–10747.
[53] Y. Wang, X. Li, Y. Chen, et al., Adv. Mater. 35 (2023) 2305257.
[54] H. Yuan, D. Jiang, Z. Li, et al., Adv. Mater. 36 (2024) 2305375.
[55] W. Wang, M. Cai, T. Wang, et al., Adv. Mater. Technol. 9 (2024) 2301607.
[56] D. Zhao, K. Sun, W.C. Cheong, et al., Angew. Chem. Int. Ed. 59 (2020) 8982–8990.
[57] W.J. Wang, H.Q. Dong, J. Lu, W. Li, L. Zhu, et al., China Powder Sci. Technol. 30 (2024) 39–50.
[58] D. Zhao, M. Hou, W. Feng, et al., Catal. Sci. Technol. 13 (2023) 4107–4116.
[59] J. Zhou, H. Liu, H. Wang, Chin. Chem. Lett. 34 (2023) 107420.
[60] S.N. Tie, W.H. Huang, Z.B. Sun, F.L. Chen, China Powder Sci. Technol. 30 (2024) 1–13.
[61] M. Hou, L. Zheng, D. Zhao, et al., Nat. Commun. 15 (2024) 1342.
[62] J. Liu, C. Lee, Y. Hu, et al., SmartMat 4 (2023) e1210.
[63] S. Shao, F. Xu, B.Q. Cao, China Powder Sci. Technol. 30 (2024) 139–149.